communications physics

ARTICLE

https://doi.org/10.1038/s42005-022-01078-9 OPEN

Electronic pair alignment and roton feature in the warm dense electron gas

Tobias Dornheim [1,2]✉, Zhandos Moldabekov [1,2], Jan Vorberger [2], Hanno Kählert[3] & Michael Bonitz[3]

The study of matter under extreme densities and temperatures as they occur, for example, in astrophysical objects and nuclear fusion applications has emerged as one of the most active frontiers in physics, material science, and related disciplines. In this context, a key quantity is given by the dynamic structure factor $S(\mathbf{q}, \omega)$, which is probed in scattering experiments—the most widely used method of diagnostics at these extreme conditions. In addition to its importance for the study of warm dense matter, the modelling of such dynamic properties of correlated quantum many-body systems constitutes an important theoretical challenge. Here, we report a roton feature in the dynamic structure factor $S(\mathbf{q}, \omega)$ of the warm dense electron gas, and introduce a microscopic explanation in terms of an electronic pair alignment model. Our results will have direct impact on the interpretation of scattering experiments and may provide insights into the dynamics of a number of correlated quantum many-body systems such as ultracold helium, dipolar supersolids, and bilayer heterostructures.

[1] Center for Advanced Systems Understanding (CASUS), Untermarkt 20, Görlitz D-02826, Germany. [2] Helmholtz-Zentrum Dresden-Rossendorf (HZDR), Bautzner Landstraße 400, Dresden D-01328, Germany. [3] Institut für Theoretische Physik und Astrophysik, Christian-Albrechts-Universität, Leibnizstraße 15, Kiel D-24098, Germany. ✉email: t.dornheim@hzdr.de

Matter at extreme densities and temperatures is ubiquitous throughout our universe[1] and naturally occurs in astrophysical objects such as giant planet interiors[2], brown dwarfs[3], and neutron stars[4]. In addition, such warm dense matter (WDM) conditions are relevant for technological applications such as the discovery of novel materials[5,6], hot-electron chemistry[7], and inertial confinement fusion[8,9]. Consequently, WDM is nowadays routinely realized in experiments in large research facilities around the globe such as the National Ignition Facility[10] in the USA, the European XFEL in Germany[11], and SACLA[12] in Japan. Indeed, the advent of new experimental techniques for the study of WDM[13] has facilitated a number of spectacular achievements[5,14–16] and has opened up new possibilities for the exciting field of laboratory astrophysics.

One of the central practical obstacles regarding the study of WDM is given by the lack of reliable diagnostics. The extreme conditions prevent the straightforward measurement even of basic system parameters like the electronic temperature, which have to be inferred indirectly from other observations. In this situation, the X-ray Thomson scattering (XRTS) technique[17] has emerged as a widely used method of diagnostics. In particular, an XRTS measurement gives one access to the dynamic structure factor (DSF) $S(\mathbf{q},\omega)$ describing the full spectrum of density fluctuations in the system. The task at hand is then to match the experimental observation with a suitable theoretical model, thereby inferring important system parameters like the electronic temperature T, density ρ, or charge state Z. Yet, the rigorous theoretical modelling of WDM[18], in general, and of an XRTS signal[19], in particular, constitutes a difficult challenge. Indeed, the physical properties of WDM are characterized by the intriguingly intricate interplay of a number of effects such as the Coulomb interaction between charged electrons and ions, partial ionization and the formation of atoms and molecules, quantum effects like Pauli blocking and diffraction, and strong thermal excitations out of the ground state.

Very recently, Dornheim et al.[20] have presented accurate results for the DSF of the uniform electron gas (UEG)[21] in the WDM regime based on ab initio path integral Monte Carlo (PIMC) simulations. In particular, the UEG assumes a homogeneous neutralizing ionic background, and, therefore, allows us to exclusively focus on the rich effects inherent to the electrons. The accurate treatment of electron–ion interactions is beyond the scope of the present work and the interested reader is referred e.g. to refs. [22,23]. The UEG constitutes one of the most fundamental model systems in physics, quantum chemistry, and related disciplines[24], and constitutes the basis for a number of important developments, such as the success of density functional theory in the description of real materials. From a practical perspective, accurate results for the DSF of the UEG are indispensable for the interpretation of WDM experiments, and directly enter models such as the widely used Chihara decomposition[17].

While the availability of highly accurate results for $S(\mathbf{q},\omega)$ constitutes an important step towards our understanding of the dynamics of correlated electronic matter, their theoretical interpretation has remained unclear. For example, the exact calculations by Dornheim et al.[20] have uncovered a negative dispersion in the UEG that closely resembles the roton feature in quantum liquids such as ^{4}He[25] and ^{3}He[26,27]. Despite speculations about a possible excitonic interpretation of this effect[28,29], its precise nature is hitherto unknown. This reflects the notorious difficulty to describe the dynamics of correlated quantum many-body systems, which constitutes a challenge in a number of research fields. In the present work, we introduce a new paradigm—the structural alignment of pairs of electrons. It allows us to understand and accurately capture both the roton feature in the strongly coupled UEG and the XC-induced red-shift of the DSF at metallic densities. Therefore, it is of substantial importance for the description and diagnostics of WDM.

Results and discussion

Spectrum of density fluctuations. In Fig. 1a, we show results for the corresponding spectrum of density fluctuations $\omega(q)$ that we estimate from the maximum in the DSF at the electronic Fermi temperature $\theta = k_B T/E_F = 1$ (with E_F being the Fermi energy) and the density parameter $r_s = \overline{a}/a_B = 10$ (with $\overline{a}$ being half the average distance to the nearest neighbour and a_B the first Bohr radius). We note that the entire depicted q-range is easily accessible in XRTS experiments at modern free electron laser facilities such as the European XFEL[11]. The dotted green curve shows the ubiquitous random phase approximation (RPA), which entails a mean-field description of the electronic density response to an external perturbation; see the 'Methods' section for details. The dash-dotted blue curve shows exact PIMC results that have been obtained on the basis of the full frequency-dependent local field correction $G(\mathbf{q}, \omega)$, which contains the complete wave-vector

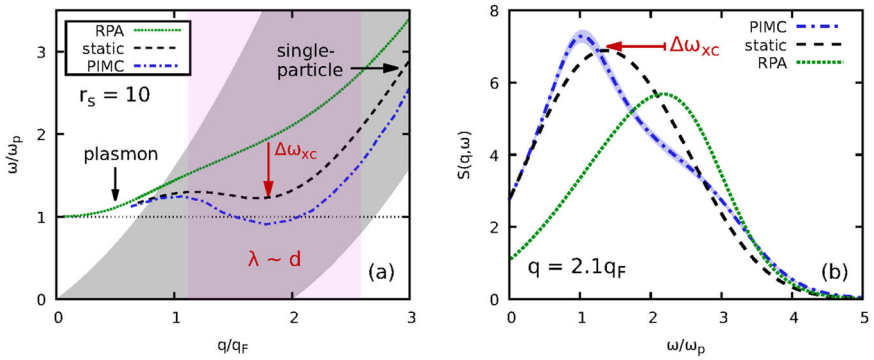

Fig. 1 Spectrum of density fluctuations of the uniform electron gas. a $\omega(q)$ at the electronic Fermi temperature ($\theta = 1$) at $r_s = 10$. Dotted green: random phase approximation; dash-dotted blue: exact path integral Monte Carlo (PIMC) results[20]; dashed black: static approximation $G(\mathbf{q}, \omega) \approx G(\mathbf{q}, 0)$. For small wave numbers, the spectrum features a single sharp plasmon excitation. This collective regime, where the wave length $\lambda = 2\pi/q$ is much larger than the average interparticle distance d, $\lambda \gg d$, is well described by the random phase approximation (RPA). Upon entering the pair continuum (shaded grey), $S(\mathbf{q}, \omega)$ becomes substantially broadened. The regime with $\lambda \sim d$ (shaded red) features a hitherto unexplained pronounced red-shift $\Delta\omega_{xc}$ compared to RPA, which eventually resembles the roton feature known from ultracold helium[26,27,35]. Finally, the single-particle regime with $q \gg q_F$ and $\lambda \ll d$ is dominated by a broad peak with $\omega(q) \sim q^2$. **b** ω-dependence of $S(\mathbf{q}, \omega)$ at $q \approx 2.1q_F$, $r_s = 10$, and $\theta = 1$. The static approximation entails an effective average over the less trivial structure of the full PIMC curve, with the shaded blue area being a measure for the uncertainty in the latter.

and frequency resolved information about electronic exchange-correlation effects. Finally, the dashed black curve corresponds to the static approximation, i.e., by setting $G(\mathbf{q}, \omega) = G(\mathbf{q}, 0)$; see Dornheim et al.[20] for a detailed explanation of the PIMC calculations.

Let us next discuss the different physical regimes shown in Fig. 1. For small q, i.e., in the collective regime where the wave length is much larger than the average interparticle distance ($\lambda \gg d \sim 2r_s$) the spectrum consists of a single, sharp plasmon peak that is exactly captured by all three theories. For completeness, we note that the plasmon is replaced by an acoustic mode in quantum liquids, and the slope is then determined by the sound speed c. Indeed, an ion acoustic mode can also be observed in realistic WDM systems, but for the (quantum) OCP there is no acoustic branch even in the limit of large r_s. Upon increasing q, we enter the pair continuum, where the plasmon decays into a multitude of other excitations and ceases to be a sharp feature[24]. From a comparison to the simulations, it is evident that the RPA breaks down in this regime and does not capture the intriguing non-monotonous behaviour of the exact PIMC data. Indeed, the latter exhibit a pronounced minimum in $\omega(q)$ around $q = 2q_F$, which closely resembles the well-known roton feature in both ^{4}He[25] and ^{3}He[26,27]. We stress that this is a real physical trend, which has been observed experimentally for electrons in alkali metals[30]. In the present work, we demonstrate that this red-shift $\Delta\omega_{xc}$ compared to RPA is a direct consequence of the alignment of pairs of electrons where $\lambda \sim d$, and show that it can be understood and accurately quantified in terms of the microscopic spatial structure of the system. Finally, a further increase of q eventually brings us into the single-particle regime ($\lambda \ll d$), where $\omega(q)$ is known to increase quadratically with q.

The static approximation leads to a substantial improvement over the RPA, and qualitatively reproduces the pronounced red-shift and even exhibits a shallow minimum in $\omega(q)$ at the correct position. A more detailed insight is given in Fig. 1b, where we show the full ω-dependence of $S(\mathbf{q}, \omega)$ in the vicinity of the roton feature. The exact PIMC curve shows a nontrivial shape consisting of a pronounced peak at $\omega(q)$ and an additional shoulder around $\omega_{RPA}(q)$. In contrast, the dashed black curve features a single broad peak that is located between both aforementioned features. In fact, the static approximation can be understood as a kind of frequency-averaged description of the actual spectrum of density fluctuations, and, therefore, reproduces frequency-averaged properties like the static structure factor $S(q)$[31] with high accuracy. Moreover, it does capture the correlation-induced shift in $S(\mathbf{q}, \omega)$ towards lower frequencies, which is the root cause of the roton feature in the UEG that is studied in the present work.

Electronic pair alignment. To understand the physical origin of the latter, it is well-worth to explore possible analogies to other systems such as ^{4}He[25] and ^{3}He[26,27]. In addition, we mention the extensively explored negative dispersion in the classical one-component plasma (OCP)[32–34]. Both cases have been explained by the onset of spatial localization of the particles[35], and the roton feature can then be quantified in terms of $S(q)$, e.g. via the Feynman ansatz[36] for He. In stark contrast, such structural arguments do not apply to the present case of the warm dense UEG. Indeed, the maximum in $S(q)$ does not exceed 1.02 even at $r_s = 10$ (see below) and the system is largely disordered.

To explain the physical mechanism behind the red-shift and eventual roton feature in the warm dense UEG, we explore the nature of the excitations of density fluctuations in this regime in Fig. 2. More specifically, the green bead depicts an arbitrary reference particle, and the blue beads other electrons which are,

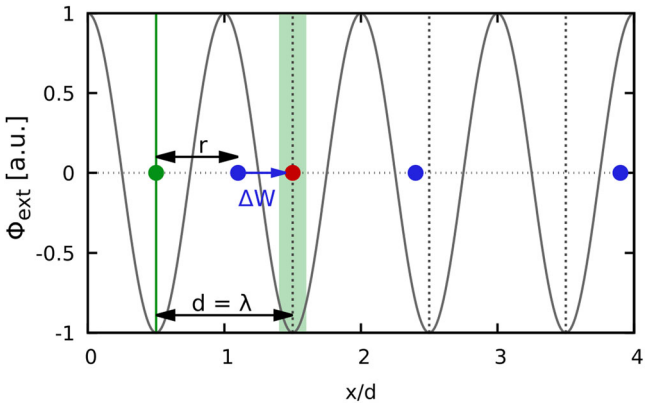

Fig. 2 Illustration of the alignment of electron pairs. Let the green bead be a fixed reference particle. Without an external perturbation [ϕ_{ext}, dark grey sinusoidal line], the system is disordered on average in the WDM regime, see the blue beads. In order to follow ϕ_{ext}, the particles have to re-align themselves to the minima of the latter, see blue arrow + red bead. In the process, they change the potential energy of the green reference particle by an amount of ΔW, see Eq. (3). In the regime of electronic pair alignment, $\lambda \sim d$, the energy shift ΔW is substantially negative. In other words, a density fluctuation with a corresponding $q = 2\pi/\lambda$ contains comparably less energy due to its alignment to the potential energy landscape of the system (shaded green area). The random phase approximation (RPA) substantially underestimates this effect and, therefore, does not capture this correlation-induced red-shift.

on average, disordered; this can be seen by the absence of pronounced features in $S(q)$. In addition, we note that the depiction of the electrons as point particles in Fig. 2 does not constitute a simplification. All quantum mechanical delocalization effects are inherently included in the evaluation of the thermodynamic expectation values within PIMC, which, in our model, enter both the effective potential and the pair correlation function in Eq. (3) below. From a mathematical perspective, the dynamic structure factor entails the same information as the density response function that describes the response to an external harmonic perturbation[24]. The latter is depicted by the black sinusoidal line and induces the leftmost blue particle to follow the perturbation, i.e., the blue arrow. This reaction of the system is associated with a change in the potential energy by an amount ΔW. In the case of $\lambda \sim d$, the particles will actually align themselves to the minima of the effective potential energy (shaded green area), which leads to a lowering of the interaction energy compared to the unperturbed case. Equivalently, we can say that a density fluctuation contains comparably less energy when $\lambda \sim d$ as it coincides with a spatial pattern that minimizes the potential energy landscape. This electronic pair alignment is highly sensitive to an accurate treatment of electronic XC-effects and becomes more pronounced with increasing r_s. It should be noted that the main purpose of Fig. 2 is the illustration of the spatial geometry of this effect; no actual perturbation of the system is assumed in our model. The exact spectrum of density fluctuations can be expressed as

$$\begin{aligned} \omega(q) &= \omega_{RPA}(q) - \Delta\omega_{xc}(q), \\ &= \omega_{RPA}(q) - \alpha(q)\Delta W_{xc}(q), \end{aligned} \tag{1}$$

where we have assumed in the second line that the kinetic contribution to $\omega(q)$ is accurately treated within RPA. The corresponding absence of XC-effects onto the momentum distribution $n(q)$ is demonstrated in the 'Methods' section. The screening coefficient[37] $\alpha(q) = \chi(q)/\chi_0(q)$ is given by the ratio of the full and noninteracting static density response functions and

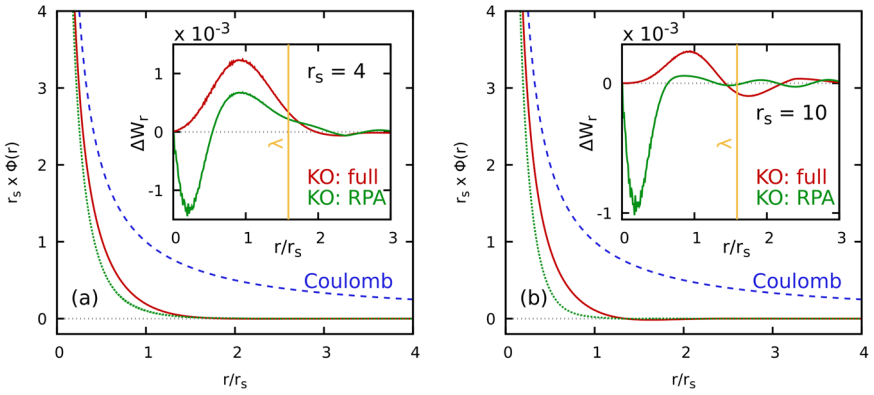

Fig. 3 Effective Kukkonen Overhauser (KO) potential between a pair of electrons surrounded by the electronic medium. Dotted green: random phase approximation (RPA); solid red: full KO potential using exact PIMC data for the local field correction (LFC) $G(\mathbf{q}, 0)$[40]; dashed blue: bare Coulomb. The inset shows the contribution $\Delta W_r(q)$ to the full shift $\Delta W(q)$ for $q \approx 2q_F$ within LFC and RPA as a function of the distance between the particles r. **a** For $r_s = 4$, positive and negative contributions to $\Delta W(q)$ approximately cancel within the RPA, and the red-shift in $\omega(q)$ is mainly due to the reduction of the interaction energy described by the exact path integral Monte Carlo (PIMC) results. **b** For $r_s = 10$, the RPA even predicts an unphysical increase of W, whereas our PIMC results again correctly describe the minimization of the interaction energy for $\lambda \sim d$.

takes into account the fact that, on the static level (i.e., in the limit of $\omega \to 0$), the UEG does not react to an external perturbation in the limit of $\lambda \gg d$. A more detailed discussion of the role of $\alpha(q)$ in our model is given below. The exchange–correlation correction to the potential part of the excitation energy of a density fluctuation of wavenumber q is given by

$$\Delta W_{\mathrm{xc}}(q) = \Delta W(q) - \Delta W_{\mathrm{RPA}}(q), \tag{2}$$

where $\Delta W(q)$ denotes the actual change in the interaction energy. Equation (1) implies that the observed red-shift in $\omega(q)$ is a direct consequence of the insufficient description of the electronic pair alignment within RPA. To quantitatively evaluate this effect, we express the energy shift ΔW as

$$\Delta W(q) = n \int \mathrm{d}\mathbf{r}\, g(r)\Big[\phi(r) - \phi(r_q)\Big], \tag{3}$$

where $\phi(r)$ denotes the effective potential between two electrons in the presence of the electron gas[38]. From a physical perspective, Eq. (3) can be interpreted as follows: a reference particle at $\mathbf{r} = \mathbf{0}$ is located in the minimum of an external sinusoidal perturbation, cf. Fig. 2. On average, it will encounter a second particle at $\mathbf{r}$ with the probability $P(\mathbf{r}) = ng(r)$, where $g(r)$ is the usual radial distribution function. Finally, we have to evaluate the difference in the effective potential between $\mathbf{r}$, and the position of the nearest minimum in the external potential, which we denote r_q. Without loss of generality, we assume a perturbation along the $\mathbf{x}$-direction. For $\lambda \gg d$, this physical picture breaks down as the translation of the second particle to r_q will be increasingly blocked by other electrons in the system. This is a direct manifestation of screening in our model, and is taken into account by the coefficient $\alpha(q)$ in Eq. (1). A relation of the energy shift Eq. (3) to the XC-contribution to the self energy known from Green functions theory is given in the 'Methods' section.

Effective electron–electron potential. The appropriate effective potential between two electrons has to 1) take into account all effects of the surrounding medium and 2) not include any XC-effects between the electrons themselves. This is a crucial difference to the effective interaction of two test charges in a medium, where one can simply use dielectric theories[24]. In the present context, the appropriate potential has been derived by Kukkonen and Overhauser[39] (KO) within linear-response theory, and is given by a functional of the local field correction (LFC), $\phi(r) = \phi[G(\mathbf{q}, 0)](r)$. Here we use exact PIMC results[40] for $G(\mathbf{q}, 0)$ and perform a Fourier transform to obtain the corresponding KO potential $\phi(r)$. The results are shown in Fig. 3 for the metallic density of $r_s = 4$ (a) and the more strongly coupled case of $r_s = 10$ (b), with the solid red, dotted green, and dashed blue lines depicting the KO potential with the LFC, the KO potential in RPA, and the bare Coulomb potential, respectively. The impact of the medium vanishes for $r \to 0$, and all curves converge. In addition, both KO potentials quickly decay for $r \gtrsim 2r_s$ and do not exhibit the long Coulombic tail. For completeness, we note that a subsequent direct PIMC study[38] of the effective potential has revealed excellent agreement to the KO expression, which further confirms the accuracy of the present results.

The insets in Fig. 3 show the respective contributions to $\Delta W(2q_F)$ [Eq. (3)], and the vertical yellow line depicts the corresponding wave length λ. For $r_s = 4$, the positive and negative contributions to ΔW_{RPA} nearly cancel. Consequently, the observed XC-induced red-shift in Fig. 4a is predominantly due to the lowering of the interaction energy, i.e., $\Delta W(q)$, in the regime of electronic pair alignment. For $r_s = 10$, the situation is more subtle, and the RPA predicts a substantial increase in $\omega(q)$ for $q \sim 2q_F$. This is a direct consequence of the pair correlation function $g_{\mathrm{RPA}}(r)$, which is known to be strongly negative for small r at these conditions. The exact PIMC results indicate a similar trend as for the metallic density and again indicate a lowering of W due to the electronic pair alignment. Therefore, it is the combination of (1) removing the spurious RPA prediction for W and (2) further adding the correct decrease in W quantified by our PIMC simulations that leads to the large down-shift of the actual $\omega(q)$ compared to RPA.

Red-shift and roton feature. Let us now apply these insights to the spectrum of density fluctuations depicted in Fig. 4. Specifically, the solid red lines show our present model Eq. (1), which reproduces the correct behaviour of $\omega(q)$ at both densities. We note that it follows the static approximation rather than the full dynamic PIMC data at $r_s = 10$. This is expected, as Eq. (3) constitutes an average over changes in the effective potential ϕ for different initial positions r. Therefore, it gives us the average change in $\omega(q)$, i.e., the location of the peak of the broad dashed black curve in Fig. 1, and not the actual position of the sharper roton peak. The predictive capability of our model is demonstrated over a broad range of densities and temperatures in the 'Methods' section.

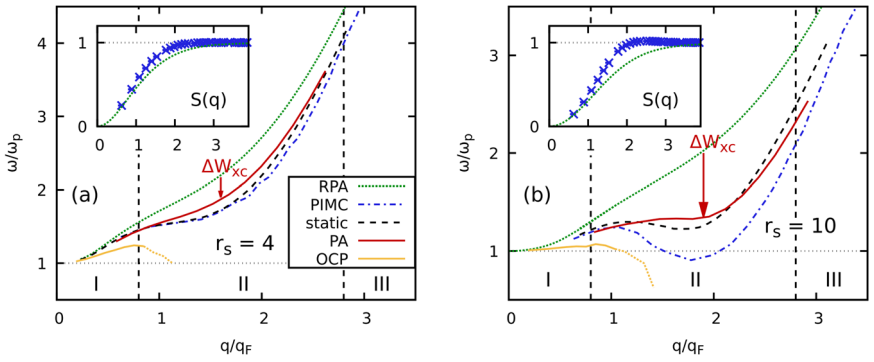

Fig. 4 Electronic pair alignment model for the spectrum of density fluctuations. Shown is the dispersion $\omega(q)$ [i.e., position of the maximum in $S(\mathbf{q}, \omega)$] of the warm dense electron gas at the electronic Fermi temperature for **a** $r_s = 4$ and **b** $r_s = 10$. Dotted green: random phase approximation (RPA); dash-dotted blue: exact path integral Monte Carlo (PIMC) results[20] using the full $G(\mathbf{q}, \omega)$; dashed black: static approximation, i.e., setting $G^{\text{static}}(\mathbf{q}, \omega) = G(\mathbf{q}, 0)$; solid yellow: classical one-component plasma (OCP) at $\Gamma = 1.92$ ($r_s = 4$) and at $\Gamma = 4.8$ ($r_s = 10$); solid red: electronic pair alignment model [Eq. (1)] introduced in this work; the red arrows indicate the corresponding average red-shift compared to RPA. We can distinguish 3 distinct physical regimes: (I) $\lambda \gg d$ [collective], (II) $\lambda \sim d$ [electronic pair alignment, two-particle excitations], and (III) $\lambda \ll d$ [single-particle]. The insets show PIMC and RPA results for the static structure factor $S(q)$ and illustrate the absence of spatial structure at these conditions.

In combination, our results provide a complete description of $\omega(q)$ over the full q-range, and allow us to give a simple and physically intuitive explanation of both the XC-induced red-shift at metallic density and the roton feature at stronger coupling. For small q, the main feature of $\omega(q)$ is given by the sharp plasmon peak. In particular, the plasmon is a collective excitation and involves all particles in the system. Upon entering the pair continuum, the DSF broadens, and we find an initial increase of $\omega(q)$ with q; this is a well-known kinetic effect due to quantum delocalization and is qualitatively reproduced by the RPA. Correspondingly, it is not present in $\omega(q)$ of the classical OCP (yellow curves in Fig. 4) at the same conditions. In the vicinity of q_F, the potential contribution to $\omega(q)$ starts to be shaped by the electronic pair alignment, and the corresponding lowering of the interaction energy W leads to the observed red-shift. In other words, the non-monotonic roton feature at $r_s = 10$ is a consequence of two competing trends: (1) the delocalization-induced quadratic increase in $\omega(q)$ and (2) the decrease of the interaction contribution due to electronic pair alignment.

An additional insight into the physical origin of the excitations in this regime comes from the effective potential shown in Fig. 3. Specifically, $\phi(r)$ vanishes for $r \gtrsim 2r_s$, which means that the change in the interaction energy W is of a distinctly local nature. This, in turn, strongly implies that the roton feature is due to two-particle excitations—the alignment of electron pairs. In this light, we can even explain the nature of the nontrivial structure of the full $S(q, \omega)$ shown in Fig. 1b: the large ΔW leading to the actual roton peak in the blue curve must be a result of configurations where two particles are initially separated by a short distance $r < r_s$. Only in this case will the corresponding change in $\phi(r)$ be sufficient for the observed lowering in $\omega(q)$. The additional shoulder in $S(q, \omega)$ is then due to transitions where the particles have even in their initial configuration been effectively separated, so that the change in $\phi(r)$ and, hence, the resulting $\Delta W(q)$ are comparably small.

Going back to Fig. 4, we note that a further increase in q again changes the nature of the excitations. In particular, $\omega(q)$ is exclusively shaped by single-particle effects when $\lambda \ll r_s$.

Conclusion

We are convinced that our findings for the spectrum of density fluctuations of the UEG—one of the most fundamental quantum systems in the literature—will open up many avenues for future research in a diverse array of fields. First and foremost, the archetypical nature of the UEG has allowed us to clearly isolate the rich interplay of the correlated electrons with each other, which constitutes an indispensable basis for the study of realistic systems. The roton feature has already been experimentally observed for electrons in metals at ambient conditions[28,30], and understanding the interplay of the electronic pair alignment with the presence of the ions will be an important next step. We expect that the observation of a non-monotonous $\omega(q)$ will also be possible in the WDM regime for real materials such as hydrogen, since the presence of bound states leads to an effectively reduced electronic density[41] and, therefore, an increased effective Wigner-Seitz radius r_s^*. Indeed, preliminary simulation results confirm that the presence of mobile ions does not weaken the roton feature but leads even to a stabilization.

Let us now return to the alternative interpretation of the roton as an excitonic mode[29]. Common to both interpretations is the governing role of short range correlations—of electron pairs or electron-hole pairs (excitons), respectively. However, in contrast to the ground state results of Takada[29], we do not find zeroes of the retarded dielectric function in the range of the roton minimum at the considered temperatures[42]. This rules out an interpretation in terms of collective modes.

Our improved microscopic theory for the DSF in the regime of $\lambda \sim d$ will be particularly relevant for the interpretation of XRTS measurements[17], which constitute the key diagnostics of state-of-the-art WDM experiments.

Going beyond the study of WDM, we stress that the proposed concept of electronic pair alignment is very general, and will likely help to shed light on the mechanism behind the spectrum of density fluctuations and elementary excitations in a number of correlated quantum systems. This includes the improved understanding of the "original" roton mode in liquid ^{4}He[25] (and the corresponding emergence of a sharp quasiparticle peak with the onset of superfluidity) and ^{3}He[26,27]. In addition, we mention the transition from the liquid regime to a highly ordered Wigner crystal[43] in strongly coupled bilayer heterostructures[44], and the impact of supersolidity[45] onto the DSF of strongly coupled dipole systems[46]. Specifically, quantum dipole systems are known to exhibit a roton feature in the DSF[35,47] and, in addition to their well-known physical realization with ultracold atoms[48], naturally emerge in electron-hole bilayer systems in the case of small layer separation.

Methods

Dynamic structure factor and density response. The dynamic structure factor $S(\mathbf{q}, \omega)$ is directly connected to the linear density response function by the well-

known fluctuation–dissipation theorem[24],

$$S(\mathbf{q},\omega) = -\frac{\mathrm{Im}\chi(\mathbf{q},\omega)}{\pi n(1-e^{-\beta\omega})}. \tag{4}$$

It is very convenient to express the latter as

$$\chi(\mathbf{q},\omega) = \frac{\chi_0(\mathbf{q},\omega)}{1-\frac{4\pi}{q^2}\left[1-G(\mathbf{q},\omega)\right]\chi_0(\mathbf{q},\omega)}, \tag{5}$$

where $\chi_0(\mathbf{q},\omega)$ describes the density response of a noninteracting system at the same conditions and can be readily computed. As we have mentioned in the main text, the dynamic LFC[37] $G(\mathbf{q},\omega)$ contains all electronic XC-effects; setting $G(\mathbf{q},\omega)\equiv 0$ thus corresponds to the RPA, which entails a mean-field description (i.e., Hartree) of the electronic density response. The DSF within RPA, the static approximation $G^{\mathrm{static}}(\mathbf{q},\omega)\equiv G(\mathbf{q},0)$, or using the full PIMC results for $G(\mathbf{q},\omega)$[20] are then obtained by inserting the corresponding $\chi(\mathbf{q},\omega)$ into Eq. (4). The DSF of the classical OCP is obtained from molecular dynamics simulations using the LAMMPS code[49].

Definition of the effective potential. The effective potential described in the main text has been first derived by Kukkonen and Overhauser[39], and is given by

$$\Phi^{\mathrm{KO}}(\mathbf{q}) = \frac{4\pi}{q^2} + \left[\frac{4\pi}{q^2}(1-G(\mathbf{q},0))\right]^2 \chi(\mathbf{q},0); \tag{6}$$

see also the excellent discussion by Giuliani and Vignale[24]. It is exclusively a functional of the LFC, and, therefore, highly sensitive to electronic XC-effects. In the present work, we use the accurate neural net representation of $G(q,\omega=0;r_s,\theta)$ by Dornheim et al.[40] that is based on exact PIMC simulation data. The results for $\phi(r)$ in coordinate space are then obtained via a simple one-dimensional Fourier transform, which we solve numerically.

Spectral representation of the DSF. An additional motivation for the present electronic pair alignment model is given by the exact spectral representation of the DSF[24],

$$S(\mathbf{q},\omega) = \sum_{m,l} P_m \left\|n_{ml}(\mathbf{q})\right\|^2 \delta(\omega-\omega_{lm}). \tag{7}$$

Here l and m denote the eigenstates of the full N-body Hamiltonian, $\omega_{lm}=(E_l-E_m)/\hbar$ is the energy difference, and n_{ml} is the usual transition element from state m to l induced by the density operator $\hat{n}(\mathbf{q})$. Equation (7) implies that $S(\mathbf{q},\omega)$ is fully defined by the possible transitions between the (time-independent) eigenstates; the full frequency dependence comes from the corresponding energy differences. In other words, no time propagation is needed. The translation of our electronic pair alignment model and the corresponding impact of $\Delta W(q)$ on $\omega(q)$ into the language of Eq. (7) is then straightforward. Firstly, we assume a continuous distribution of eigenstates, which we examine in coordinate space. In the regime of $\lambda \sim d$, the excitations primarily involve only two particles, as the effective potential $\phi(r)$ decays rapidly with r. The probability $P(r)=ng(r)$ thus plays the role of P_m in Eq. (7), and the energy shift can be expressed as $\omega_{lm}=\Delta W_{lm}+\Delta K_{lm}$. The kinetic contribution is accurately captured by the RPA as we demonstrate in the next section. Finally, we note that Eq. (7) even gives us some insight into the nontrivial shape of the exact PIMC results for $S(\mathbf{q},\omega)$ shown in Fig. 1 in the main text. In particular, the roton peak around ω_{p} must be due to transitions where the downshift ΔW is substantial. This is only the case for electron pairs that have been separated by $r<r_s$ in the initial state. The substantial reduction in the interaction energy of such a pair due to an excitation with $\lambda\sim d$ is thus the microscopic explanation for the observed roton feature.

Momentum distribution of the correlated electron gas. In Fig. 5, we show the momentum distribution function $n(k)$ of the UEG at the electronic Fermi temperature $\theta=1$. Specifically, the symbols show exact PIMC results[50] for different values of r_s, and the dashed black line the Fermi distribution describing a noninteracting Fermi gas at the same conditions. Clearly, $n(k)$ is hardly influenced by the Coulomb interaction for both $r_s=4$ (blue diamonds) and $r_s=10$ (green crosses); correlation effects only manifest for much larger r_s, cf. the yellow triangles that have been obtained for a strongly coupled electron liquid ($r_s=50$). This is a strong indication that the main error in $\omega_{\mathrm{RPA}}(q)$ is due to ΔW and not the kinetic part.

Results for other temperatures and densities. In the main text, we have restricted ourselves to the representative cases of $r_s=4$ (metallic density) and $r_s=10$ (boundary to the electron liquid regime[21]) at the electronic Fermi temperature, $\theta=k_{\mathrm{B}}T/E_{\mathrm{F}}$. The validity of our electronic pair alignment model is demonstrated for a vast range of densities and temperatures in Fig. 6.

Connection of the electronic pair alignment model to Green functions theory. In the following, we connect the shift of the plasmon dispersion to the energy change of a test particle, ΔW_{xc}. Kwong and Bonitz[51] have derived a direct relation between the DSF and the single-particle nonequilibrium Green function (NEGF) $\delta G^<$ that is produced by a short monochromatic field pulse, $U(t,q)=U_0(t)\cos qx$,

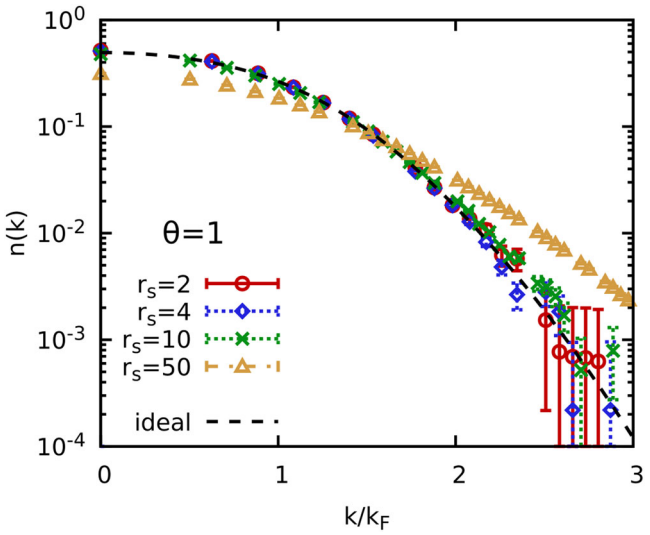

Fig. 5 Momentum distribution $n(k)$ of the uniform electron gas at the electronic Fermi temperature $\theta=1$. The symbols show exact path integral Monte Carlo (PIMC) results for $r_s=2$ (red circles), $r_s=4$ (blue diamonds), $r_s=10$ (green crosses), and $r_s=50$ (yellow triangles); the dashed black line shows the Fermi distribution function describing a noninteracting Fermi gas. Taken from Dornheim et al.[50], and reproduced with the permission of the American Physical Society.

and is valid in case of a weak excitation (linear response). Here we rewrite this in terms of the spectral function of the occupied states, δA,

$$S(\omega,q) = \frac{1}{\pi n_0 \hbar U_0(\omega)} \sum_p \delta A(p,\omega,U), \tag{8}$$

$$\delta A(p,\omega,U) = A(p,\omega,U) - A(p,\omega,0), \tag{9}$$

where the argument U comprises the dependencies on U_0 and q. Note that δA is proportional to U_0, cancelling its appearance in the denominator. Thus, in linear response there is a direct linear relation between the frequency dependencies of the DSF and the field-induced correction to the single-particle spectral function. Now the question is how the peak position of the DSF, $\omega(q)$, that is discussed in the main part of the paper, is related to the peak position $\delta E(p,U)$ of the spectral function δA.

To answer this question we follow the approach by Kwong and Bonitz[51] and outline the main steps. First the Keldysh-Kadanoff-Baym equations (KBE) are solved for the NEGF, $G(t_1,t_2)$, in the two-time plane, in the presence of the field U. The spectral information is then contained in the dependence of $A(p,\tau,U)$ on the difference time, $\tau=t_1-t_2$, and the numerical result can be expressed as a Fourier series

$$A(p,\tau,U) = \sum_a C_a e^{i\frac{E_a(p)}{\hbar}\tau} e^{-\Gamma_a(p)\tau}. \tag{10}$$

The exponential damping ansatz is known to be a poor approximation for small τ, and can be straightforwardly improved; however, for the present discussion ansatz (10) is sufficient.

In the field-free case, $U_0\to 0$, and a given exchange-correlation self energy of the uniform electron gas, $\Sigma_{xc}(p,\tau)$ [the Hartree term vanishes for the UEG], the sum (10) contains only a small number s of terms. For example, in the quasiparticle approximation, there is only one term, $s=1$, with $E_1(p)=\frac{p^2}{2m}+\mathrm{Re}\,\Sigma_{xc}(p,\tau)$ and $\hbar\Gamma_1(p)=\mathrm{Im}\,\Sigma_{xc}(p,\tau)$. Since the system is stationary, there is no dependence on the center of mass time, $T=(t_1+t_2)/2$. Now, when the field U is turned on, it excites plasma oscillations with wavenumber q which give rise to one additional contribution to the sum with (within linear response)

$$E_2(p,q) = \delta\Sigma_H(p,q) + \mathrm{Re}\,\delta\Sigma_{xc}(p,q), \tag{11}$$

$$\hbar\Gamma_2(p,q) = \mathrm{Im}\,\delta\Sigma_{xc}(p,q), \tag{12}$$

where $\delta\Sigma_H$ and $\delta\Sigma_{xc}$ are the linear perturbations of the selfenergies due to the external field, where we suppress the time dependencies. The specific contribution to the single-particle spectrum that is caused by plasmons can be isolated by considering the difference δA, where s field-free terms cancel. Now, Fourier transforming with respect to τ yields a Lorentzian in frequency space with the peak position of $\delta A(p,\omega)$ given by $E_2(p,q)=\delta E(p,q)$,

$$\delta E(p,q) \approx \delta\Sigma_H(p,q) + \mathrm{Re}\,\delta\Sigma_{xc}(p,q), \tag{13}$$

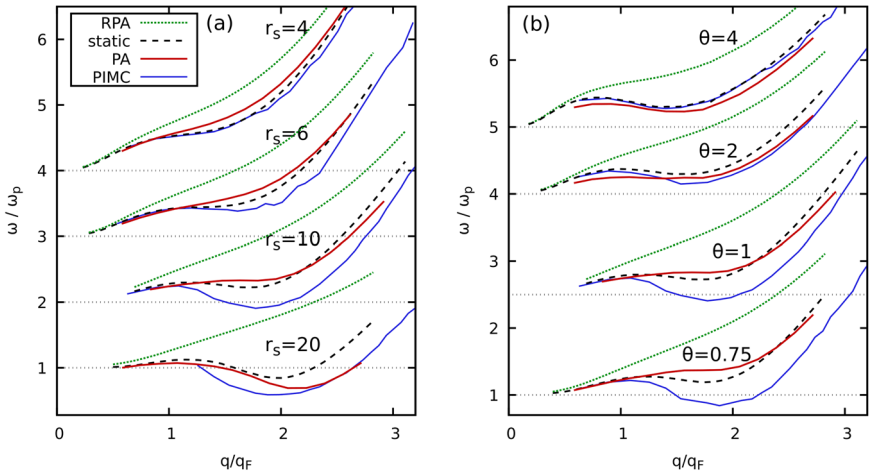

Fig. 6 Wavenumber dependence of the spectrum of density fluctuations $\omega(q)$ at different conditions. Dotted green: random phase approximation (RPA); dashed black: static approximation; solid blue: exact path integral Monte Carlo (PIMC) results[20]; solid red: electronic pair alignment model [Eq. (1)] introduced in this work. **a** Results for different values of the density parameter r_s at $\theta = 1$; **b** results for different values of the temperature parameter $\theta = k_B T/E_F$ for $r_s = 10$.

with the life time Γ_2. If the KBE are solved in the presence of the field on the mean-field level ($\Sigma_{xc} = 0$), the second term in Eq. (13) vanishes which is known to yield the plasmon spectrum (peak of the DSF) on RPA-level, $\omega_{\rm RPA}(q)$[51]. If exchange-correlation effects are restored, the plasmon spectrum and energy spectrum δE undergo synchronous changes,

$$\begin{aligned}&\omega_{\rm RPA}(q) \to \omega(q)\\ &\delta\Sigma_H(p,q) \to \delta\Sigma_H(p,q) + {\rm Re}\,\delta\Sigma_{xc}(p,q).\end{aligned} \tag{14}$$

Equivalently, we may subtract the terms on the left-hand side. This yields, on one hand, the frequency change, $\Delta\omega_{\rm xc} = \omega(q) - \omega_{\rm RPA}(q)$, that is caused by exchange-correlation effects. On the other hand, this leads to the xc-induced difference of energy dispersions

$$\Delta\delta E_{\rm xc}(p,q) \approx {\rm Re}\,\delta\Sigma_{\rm xc}(p,q). \tag{15}$$

Thus, we have established a direct link between the two exchange-correlation energy effects, $\Delta\omega_{\rm xc}$ and ${\rm Re}\,\delta\Sigma_{\rm xc}(p,q)$. Taking into account the linear relation (8) and subtracting the mean field (RPA) expressions, we expect a proportionality also for the peak positions,

$$\Delta\omega_{\rm xc}(q) \sim \sum_p {\rm Re}\,\delta\Sigma_{\rm xc}(p,q) \tag{16}$$

While, the KBE procedure has been successfully demonstrated for the computation of the plasmon spectrum[51], the change of the single-particle energy, Eq. (15), is presently not available. Physically, $\delta\Sigma_{\rm xc}(p,q)$ has the meaning of the field-induced change of the energy of a test particle that is related to its interaction with the medium[41]. Since ΔW_{xc} has exactly this meaning (an approximation to it) we conclude that

$$\sum_p \Delta\delta E_{\rm xc}(p,q) \sim \Delta W_{\rm xc}(q). \tag{17}$$

Together with the proportionality (16) this gives a connection to Eq. (1) of the main text.

Data availability

The neural network representation of the static local field correction is available in Dornheim et al.[40]. All further data that support the findings of this study are available from the corresponding author upon reasonable request.

Received: 14 April 2022; Accepted: 4 November 2022;
Published online: 27 November 2022

References

1. Fortov, V. E. Extreme states of matter on earth and in space. *Phys.-Usp* **52**, 615–647 (2009).
2. Benuzzi-Mounaix, A. et al. Progress in warm dense matter study with applications to planetology. *Phys. Scripta* **T161**, 014060 (2014).
3. Becker, A. et al. Ab initio equations of state for hydrogen (H-REOS. 3) and helium (He-REOS. 3) and their implications for the interior of brown dwarfs. *Astrophys. J. Suppl. Ser* **215**, 21 (2014).
4. Haensel, P., Potekhin, A. Y. & Yakovlev, D. G. (eds). *Equilibrium Plasma Properties. Outer Envelopes* 53–114 (Springer New York, 2007).
5. Kraus, D. et al. Nanosecond formation of diamond and lonsdaleite by shock compression of graphite. *Nat. Commun.* **7**, 10970 (2016).
6. Lazicki, A. et al. Metastability of diamond ramp-compressed to 2 terapascals. *Nature* **589**, 532–535 (2021).
7. Brongersma, M. L., Halas, N. J. & Nordlander, P. Plasmon-induced hot carrier science and technology. *Nat. Nanotechnol.* **10**, 25–34 (2015).
8. Hu, S. X., Militzer, B., Goncharov, V. N. & Skupsky, S. First-principles equation-of-state table of deuterium for inertial confinement fusion applications. *Phys. Rev. B* **84**, 224109 (2011).
9. Betti, R. & Hurricane, O. A. Inertial-confinement fusion with lasers. *Nat. Phys.* **12**, 435–448 (2016).
10. Zylstra, A. B. et al. Burning plasma achieved in inertial fusion. *Nature* **601**, 542–548 (2022).
11. Tschentscher, T. et al. Photon beam transport and scientific instruments at the European XFEL. *Appl. Sci.* **7**, 592 (2017).
12. Pile, D. First light from sacla. *Nat. Photon.* **5**, 456–457 (2011).
13. Falk, K. Experimental methods for warm dense matter research. *High Power Laser Sci. Eng* **6**, e59 (2018).
14. Fletcher, L. B. et al. Ultrabright x-ray laser scattering for dynamic warm dense matter physics. *Nat. Photon.* **9**, 274–279 (2015).
15. Kraus, D. et al. Formation of diamonds in laser-compressed hydrocarbons at planetary interior conditions. *Nat. Astron.* **1**, 606–611 (2017).
16. Knudson, M. D. et al. Direct observation of an abrupt insulator-to-metal transition in dense liquid deuterium. *Science* **348**, 1455–1460 (2015).
17. Glenzer, S. H. & Redmer, R. X-ray Thomson scattering in high energy density plasmas. *Rev. Mod. Phys* **81**, 1625 (2009).
18. Graziani, F., Desjarlais, M. P., Redmer, R. & Trickey, S. B. (eds). *Frontiers and Challenges in Warm Dense Matter* (Springer, International Publishing, 2014).
19. Mo, C. et al. First-principles method for x-ray Thomson scattering including both elastic and inelastic features in warm dense matter. *Phys. Rev. B* **102**, 195127 (2020).
20. Dornheim, T., Groth, S., Vorberger, J. & Bonitz, M. Ab initio path integral Monte Carlo results for the dynamic structure factor of correlated electrons: from the electron liquid to warm dense matter. *Phys. Rev. Lett.* **121**, 255001 (2018).
21. Dornheim, T., Groth, S. & Bonitz, M. The uniform electron gas at warm dense matter conditions. *Phys. Reports* **744**, 1–86 (2018).
22. Fortmann, C., Wierling, A. & Röpke, G. Influence of local-field corrections on Thomson scattering in collision-dominated two-component plasmas. *Phys. Rev. E* **81**, 026405 (2010).
23. Simoni, J. & Daligault, J. First-principles determination of electron-ion couplings in the warm dense matter regime. *Phys. Rev. Lett.* **122**, 205001 (2019).
24. Giuliani, G. & Vignale, G. *Quantum Theory of the Electron Liquid* (Cambridge University Press, 2008).
25. Griffin, A. et al. *Excitations in a Bose-condensed Liquid. Cambridge Studies in Low Temperature Physics* (Cambridge University Press, 1993).
26. Godfrin, H. et al. Observation of a roton collective mode in a two-dimensional Fermi liquid. *Nature* **483**, 576–579 (2012).

27. Dornheim, T., Moldabekov, Z. A., Vorberger, J. & Militzer, B. Path integral Monte Carlo approach to the structural properties and collective excitations of liquid ^{3}he without fixed nodes. *Sci. Rep.* **12**, 708 (2022).
28. Takada, Y. & Yasuhara, H. Dynamical structure factor of the homogeneous electron liquid: its accurate shape and the interpretation of experiments on aluminum. *Phys. Rev. Lett.* **89**, 216402 (2002).
29. Takada, Y. Emergence of an excitonic collective mode in the dilute electron gas. *Phys. Rev. B* **94**, 245106 (2016).
30. vom Felde, A., Sprösser-Prou, J. & Fink, J. Valence-electron excitations in the alkali metals. *Phys. Rev. B* **40**, 10181–10193 (1989).
31. Dornheim, T. et al. Effective static approximation: a fast and reliable tool for warm-dense matter theory. *Phys. Rev. Lett.* **125**, 235001 (2020).
32. Mithen, J. P., Daligault, J. & Gregori, G. Onset of negative dispersion in the one-component plasma. in *AIP Conference Proceedings* Vol. 1421, 68–72 (2012).
33. Arkhipov, Y. V. et al. Direct determination of dynamic properties of coulomb and Yukawa classical one-component plasmas. *Phys. Rev. Lett.* **119**, 045001 (2017).
34. Arkhipov, Y. V. et al. Dynamic characteristics of three-dimensional strongly coupled plasmas. *Phys. Rev. E* **102**, 053215 (2020).
35. Kalman, G. J., Hartmann, P., Golden, K. I., Filinov, A. & Donkó, Z. Correlational origin of the roton minimum. *Europhys. Lett.* **90**, 55002 (2010).
36. Feynman, R. P. & Cohen, M. Energy spectrum of the excitations in liquid helium. *Phys. Rev.* **102**, 1189–1204 (1956).
37. Kugler, A. A. Theory of the local field correction in an electron gas. *J. Stat. Phys* **12**, 35 (1975).
38. Dornheim, T., Tolias, P., Moldabekov, Z. A., Cangi, A. & Vorberger, J. Effective electronic forces and potentials from ab initio path integral Monte Carlo simulations. *J. Chem. Phys.* **156**, 244113 (2022).
39. Kukkonen, C. A. & Overhauser, A. W. Electron-electron interaction in simple metals. *Phys. Rev. B* **20**, 550–557 (1979).
40. Dornheim, T. et al. The static local field correction of the warm dense electron gas: an ab initio path integral Monte Carlo study and machine learning representation. *J. Chem. Phys* **151**, 194104 (2019).
41. Kremp, D., Schlanges, M. & Kraeft, W.-D. *Quantum Statistics of Nonideal Plasmas* (Springer, 2005).
42. Hamann, P., Vorberger, J., Dornheim, T., Moldabekov, Z. A. & Bonitz, M. Ab initio results for the plasmon dispersion and damping of the warm dense electron gas. *Contrib. Plasma Phys.* **60**, e202000147 (2020).
43. Zhou, Y. et al. Bilayer Wigner crystals in a transition metal dichalcogenide heterostructure. *Nature* **595**, 48–52 (2021).
44. Du, L. et al. Engineering symmetry breaking in 2d layered materials. *Nature Reviews Physics* **3**, 193–206 (2021).
45. Saccani, S., Moroni, S. & Boninsegni, M. Excitation spectrum of a supersolid. *Phys. Rev. Lett.* **108**, 175301 (2012).
46. Navon, N., Smith, R. P. & Hadzibabic, Z. Quantum gases in optical boxes. *Nature Physics* **17**, 1334–1341 (2021).
47. Filinov, A., Prokof'ev, N. V. & Bonitz, M. Berezinskii-Kosterlitz-Thouless transition in two-dimensional dipole systems. *Phys. Rev. Lett.* **105**, 070401 (2010).
48. Ni, K. K., Ospelkaus, S., Nesbitt, D. J., Ye, J. & Jin, D. S. A dipolar gas of ultracold molecules. *Phys. Chem. Chem. Phys.* **11**, 9626–9639 (2009).
49. Plimpton, S. Fast parallel algorithms for short-range molecular dynamics. *J. Comput. Phys.* **117**, 1–19 (1995).
50. Dornheim, T., Böhme, M., Militzer, B. & Vorberger, J. Ab initio path integral Monte Carlo approach to the momentum distribution of the uniform electron gas at finite temperature without fixed nodes. *Phys. Rev. B* **103**, 205142 (2021).
51. Kwong, N.-H. & Bonitz, M. Real-time Kadanoff-Baym approach to plasma oscillations in a correlated electron gas. *Phys. Rev. Lett.* **84**, 1768–1771 (2000).

Acknowledgements

This work was partly funded by the Center for Advanced Systems Understanding (CASUS) which is financed by Germany's Federal Ministry of Education and Research (BMBF) and by the Saxon Ministry for Science, Culture and Tourism (SMWK) with tax funds on the basis of the budget approved by the Saxon State Parliament. M.B. acknowledges support by the DFG via project BO1366/15. The PIMC calculations were carried out at the Norddeutscher Verbund für Hoch- und Höchstleistungsrechnen (HLRN) under grant shp00026 and on a Bull Cluster at the Center for Information Services and High Performance Computing (ZIH) at Technische Universität Dresden.

Author contributions

T.D. developed the original idea, produced all graphics, and substantially contributed to writing the manuscript. Z.M. and J.V. contributed to the analysis and to writing the manuscript. H.K. carried out classical MD simulations and contributed to writing the manuscript. M.B. developed the Green functions theory, and contributed to the analysis and to writing the manuscript.

Funding

Open Access funding enabled and organized by Projekt DEAL.

Competing interests

The authors declare no competing interests.

Additional information

Supplementary information The online version contains supplementary material available at https://doi.org/10.1038/s42005-022-01078-9.

Correspondence and requests for materials should be addressed to Tobias Dornheim.

Peer review information *Communications Physics* thanks the anonymous reviewers for their contribution to the peer review of this work. Peer reviewer reports are available.

Reprints and permission information is available at http://www.nature.com/reprints

Publisher's note Springer Nature remains neutral with regard to jurisdictional claims in published maps and institutional affiliations.